2025 SCEC Report: SCEC Project 25313

Physics-based modeling of postseismic slip in the complex Ridgecrest fault system using Tandem

Alice-Agnes Gabriel, **Yohai Magen**, Dave A. May, and Jeena Yun

Funding	Organization Budget	Investigators	Funded
	University of California, San Diego	Alice-Agnes Gabriel, Yohai Magen, Dave A. May, Jeena Yun, Piyush Karki	$24,241

Category B: Collaborative Research Project **Science Milestones:** C1,2,3-1, C2-1, C2-2
Community Models: CFM, CSM, CTM, CVM

Abstract: The July 6, 2019, Mw 7.1 Ridgecrest earthquake ruptured a geometrically complex fault system in the Eastern California Shear Zone, extending from the Garlock fault in the south to the Coso geothermal region in the north. Recent observations of Ridgecrest's post-seismic deformation, captured by Sentinel-1 Burst Overlap Interferometry (BOI; *Magen et al., 2024*) and GNSS data, reveal a strong correlation between displacement rates and proximity to Coso's geothermal field, also reflected in the spatio-temporal distribution of post-seismic seismicity. These findings suggest that elevated heat flow plays a significant role in controlling fault frictional properties and accelerating aseismic slip. This project developed a physics-based 3D model of the post-seismic kinematics of the Mw 7.1 Ridgecrest earthquake, focusing on the effects of complex multi-fault geometry and frictional heterogeneity. We use Tandem (*Gabriel et al., 2026*), an HPC-optimized discontinuous Galerkin code to simulate Sequences of Earthquakes and Aseismic Slip (SEAS), to model aseismic slip across the Ridgecrest fault system. We first benchmarked Tandem against the SCEC SEAS BP7 community exercise, then developed a postseismic afterslip model that fits both BOI and GNSS observations and indicates that along-strike variations in rate-and-state friction parameters, modulated by Coso's heat flow, can explain the observed deformation. To assess the contribution of viscoelastic relaxation, we extended Tandem with a Maxwell viscoelastic rheology, validated against the Savage and Prescott (1978) analytical solution.

Intellectual Merit: This project advanced physics-based modeling of postseismic deformation by integrating high-resolution geodetic observations with 3D rate-and-state friction simulations of a complex multi-fault system. We demonstrate that along-strike variations in frictional properties, plausibly linked to elevated heat flow near the Coso geothermal region, can quantitatively reproduce both BOI and GNSS observations of postseismic displacement following the 2019 Mw 7.1 Ridgecrest earthquake. Tandem successfully passed the SCEC SEAS BP7 community benchmark, providing a verified, scalable, volumetric simulation tool for the SCEC community. We extended Tandem to support Maxwell viscoelastic rheology, validated against the Savage and Prescott (1978) analytical solution, enabling future investigations of coupled afterslip and viscoelastic relaxation in regions with complex thermo-mechanical structure.

Broader Impacts: This award supported research training of an early-career postdoctoral scholar (Yohai Magen) and a graduate student (Jeena Yun) at SIO/UCSD. In addition, Piyush Karki, a Computer Science PhD student at LMU and TUM in Munich, Germany, led the viscoelasticity implementation. Tandem v1.2, with new viscoelastic capabilities, normal- and shear-stress perturbations, HDF5 I/O, scalable Green's function checkpointing, and an additional friction law, will be released open-source to the SCEC and broader earthquake-modeling community. The project's findings on the role of geothermal heat flow in modulating fault frictional behavior have implications for postseismic hazard assessment in California regions with complex geothermal-fault interactions and provide a transferable framework for analyzing afterslip following large earthquakes.

Detailed Project Report

1. Tandem 3D Benchmarking against the SCEC SEAS BP7 Exercise

Tandem participated in the SCEC SEAS community benchmark BP7 (*Lambert et al., 2023*), which models a circular velocity-weakening (VW) nucleation zone embedded in a 3D, homogeneous, isotropic, elastic whole space. The benchmark consists of a planar rate-and-state fault on which a smooth stress perturbation triggers the first rupture. Tandem achieves good agreement with the boundary-integral code BiCyclE (*Lapusta et al., 2000; Lapusta and Liu, 2009*) and the finite-difference code Thrase (*Erickson and Dunham, 2014*) in these large-scale 3D SEAS simulations (Fig. 1). The slight mismatch in recurrence interval for the aging law is consistent with previous benchmark results and reflects the impact of varying domain size and boundary conditions in volumetric codes, as well as sensitivity to numerical choices (*Jiang et al., 2022*). Comparing the evolution of the first earthquake, the slip-law event grows initially slower and then outpaces the aging-law rupture, with both fully rupturing the VW patch after ~1.8 s.

To approximate the unbounded whole-space solution with a volumetric code, we embed the 0.8×0.8 km rate-and-state fault in a 2×2×2 km domain and impose constant tectonic loading via Dirichlet boundaries (surfaces parallel to the z-axis), treating the remaining faces as traction-free. We use polynomial degree 3 for the discontinuous Galerkin basis, with on-fault element size of 0.03 km in the VW region and gradual coarsening toward the boundaries. This setup yields 4,698 tetrahedral elements, 2,446 of which have a face on the fault surface. Across the four BP7 quasi-dynamic scenarios, Tandem requires ~1,350-2,026 CPU hours on 60 AMD EPYC 7662 processors.

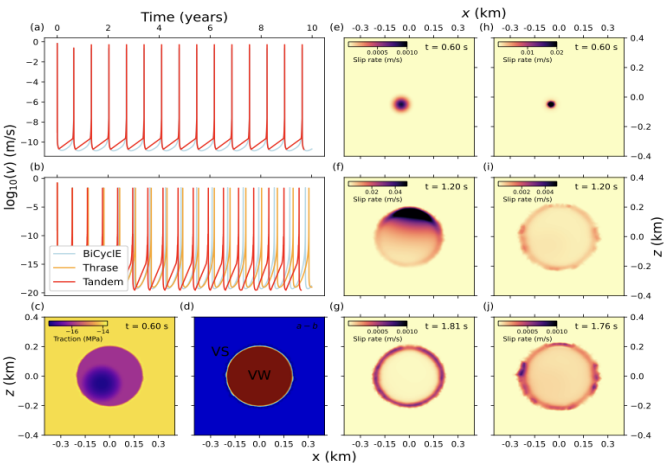

Figure 1. *Benchmark comparison demonstrating that Tandem reproduces key results for the SCEC SEAS benchmark BP7 (Lambert et al., 2023). Tandem (this study) is compared to BiCyclE (Lapusta et al., 2000; Lapusta and Liu, 2009) and Thrase (Erickson and Dunham, 2014). (a) Slip-rate time series at the center of the VW patch for the slip law. (b) Same as (a) for the aging law. (c) Shear traction on the fault at t = 0.6 s, with the first rupture initiated by a smooth stress perturbation centered at (x, z) = (−0.05, −0.05) km. (d) Distribution of (a − b) along the fault, with (a − b) = ±0.006 in the VW and velocity-strengthening (VS) regions. (e–g) Snapshots of the first rupture under the aging law and (h–j) under the slip law. From Gabriel et al. (2025, Figure 4).*

2. 3D Postseismic Simulations of the Mw 7.1 Ridgecrest Earthquake

We modeled the Ridgecrest postseismic response using a rate-and-state friction, aging-law-governed fault in Tandem (*Uphoff et al., 2023*). Initial conditions for the postseismic phase were sampled from a 3D dynamic rupture model of the coseismic phase (*Taufiqurrahman et al., 2023*). For portions of the fault not covered by the coseismic dynamic model (down-dip and northward toward Coso), we assume velocity-strengthening (VS) behavior with steady-state slip rate and state variable; stress changes are computed from the coseismic slip distribution using Okada's dislocations. To capture the observed seismicity and deformation rate variations as a function of distance to the Coso volcanic region, we vary the difference between the direct-effect parameter (a) and the evolution-effect parameter (b) on the VS portion of the fault.

We fix b = 0.04 and parameterize a as a spatially variable function of depth (d) and along-strike distance (y). In the central coseismic region, a baseline value of 0.03 is imposed. To account for the faster decay of deformation and seismicity toward Coso, we additionally let the VS-VW transition shallow toward Coso, following the background seismicity, with a 14 km transition depth in the coseismic region and 4 km near Coso. The rate-and-state direct-effect parameter varies linearly along strike as $a = a_m y + a_{max}$. Across our suite of simulations, we systematically varied a_{max} and a_m to test different along-strike frictional profiles.

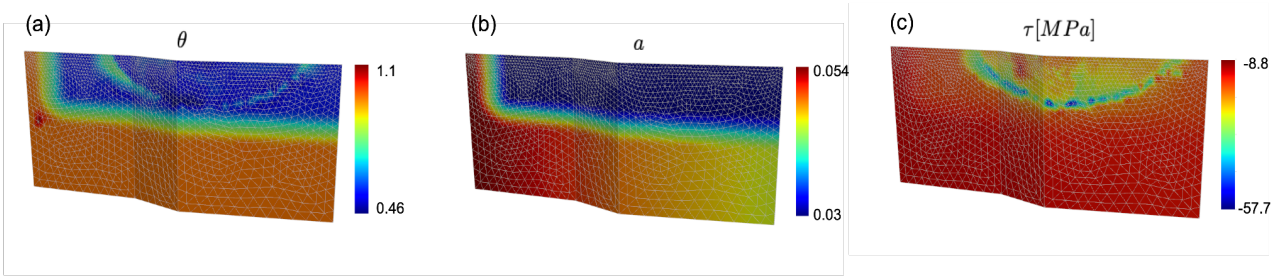

Figure 2. *Initial conditions for the rate-and-state afterslip model. (a) Initial state variable, (b) example of the spatially variable initial frictional properties used across simulations, (c) initial shear stress.*

3. Data Integration and Validation against Observations

To find the linear-ramp direct-effect parameterization that best fits the observations, we conducted a grid search over a_{max} and a_m. At each grid point, model surface displacements were compared with the temporal deformation field from GNSS daily solutions (Nevada Geodetic Laboratory; Blewitt et al., 2018) and BOI data (Magen et al., 2024), and the mean-square errors were computed.

Varying the direct-effect parameter as a function of distance from Coso explains the temporal behavior of both deformation and aftershocks. The best-fitting physics-based rate-and-state afterslip model achieves a 75% variance reduction relative to the BOI data and a 92% variance reduction relative to GNSS (Figure 3). These results support the interpretation that the spatio-temporal distribution of postseismic deformation is largely controlled by along-strike variations in frictional properties driven by crustal mechanics and heat flow. Although our purely elastic afterslip model captures the observed deformation, it does not account for viscoelastic relaxation. Background seismicity indicates a much shallower brittle-ductile transition beneath Coso (~4 km) compared with the main Ridgecrest coseismic zone (~14 km; Im et al.). Viscoelasticity therefore cannot be ruled out as a contributor; we address this in Section 4.

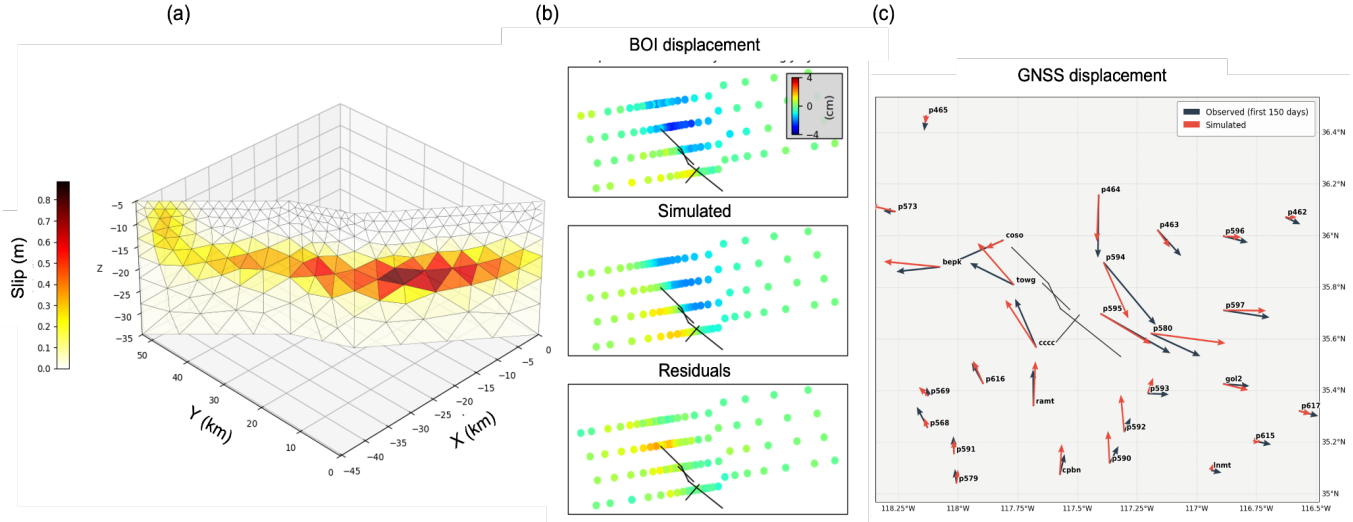

Figure 3. *Postseismic slip distribution and first 150-day displacement data fit. (a) Cumulative postseismic slip during the first 150 days following the Ridgecrest earthquake, (b) fit to BOI data, and (c) fit to GNSS data.*

4. Tandem Viscoelasticity Implementation

To simulate the viscoelastic response of the crust, we extended the Tandem framework (*Uphoff et al., 2023; Gabriel et al., 2026*) to incorporate a Maxwell viscoelastic rheology (Standard Linear Solid). Our implementation separates the stress and strain tensors into volumetric and deviatoric components, enabling us to independently track the viscous evolution based on the material's characteristic decay time (*Gharti et al., 2019*). The numerical core of this development reformulates the constitutive relations to decouple the unknown current displacement field from the time-dependent "history" of previous strains. By isolating these historical strain components, the time-evolving viscous effects are moved to the right-hand side of the discontinuous Galerkin weak formulation, integrating cleanly with Tandem's existing solver and computational kernels.

We validated the new viscoelastic capability against the *Savage and Prescott (1978)* analytical solution for repeated strike-slip earthquakes. Our 3D finite-element setup mirrors the 2D analytical model: a Maxwell viscoelastic layer is underlain by an elastic layer, with a fault divided into a locked upper seismogenic zone and a continuously creeping lower section. We impose Dirichlet conditions on the fault and lateral domain boundaries, free-surface conditions on the top and bottom, and free slip at the boundary between the fault and the viscoelastic layer. A comparison of fault-perpendicular surface deformation profiles during the first, fifth, and tenth modeled earthquake cycles (Figure 4) demonstrates excellent agreement with the analytical solution following an initial spin-up phase.

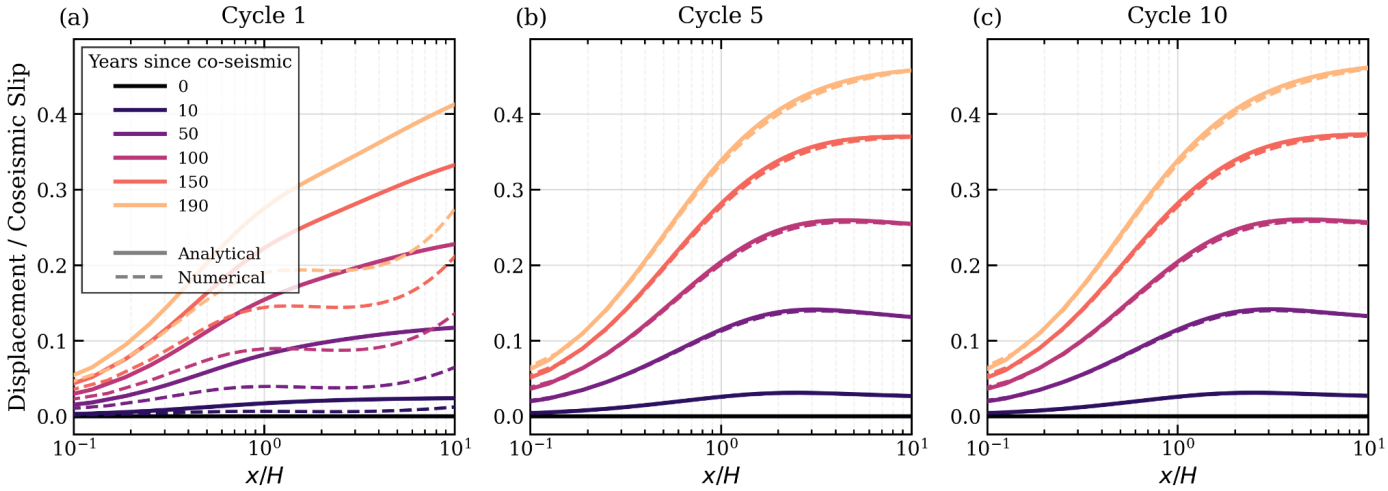

Figure 4. *Comparison of the analytical solution of Savage and Prescott (1978) with the new Tandem viscoelastic solver. Viscoelastic response following the first (a), fifth (b), and tenth (c) earthquake cycle. The x-axis is normalized by the seismogenic width and the y-axis by the imposed coseismic slip.*

5. Tandem Software Developments

The Tandem team is preparing the release of version 1.2. The new release supports fully scalable discrete Green's function checkpointing, time-integration checkpointing, an additional friction law, perturbations in normal and shear stresses, reparameterization of the rate-and-state friction solve, and flexible HDF5 I/O. Together these features enable substantial numerical speed-ups without compromising the underlying physics, improve robustness, facilitate integration with other community codes, and broaden the range of accessible problems. A detailed description of the new features and verification is provided in *Gabriel et al. (2026).*

Publications Acknowledging this Award

1. Magen, Y., May, D. A., & Gabriel, A.-A. (2026). Reduced-order modelling of Cascadia's slow slip cycles. Geophysical Journal International, 245(2), ggag050. doi:10.1093/gji/ggag050.

2. Gabriel, A.-A., Karki, P., Magen, Y., Oryan, B., Ulrich, T., Yun, J., & May, D. A. (2026). Tandem: An Open-Source High-Performance Computing Volumetric Software to Model Sequences of Earthquakes and Aseismic Slip Across Complex Fault Systems. Seismological Research Letters (in press). EarthArXiv preprint: doi:10.31223/X5V75G

Preprints and Manuscripts in Preparation

1. Magen, Y., Gabriel, A.-A., & May, D. A. (2026). Along-strike coupling heterogeneity in Cascadia's slow-slip zone constrained by GNSS and reduced-order rate-and-state friction modeling. EarthArXiv. doi:10.31223/x5df3r.
2. Yun, J., Fialko, Y., May, D. A., Gabriel, A.-A., Williams, C. A., & Liu, D. (in preparation). Effects of loading schemes in simulations of Sequences of Earthquakes and Aseismic Slip (SEAS) using volumetric methods.

SCEC Conference Presentations Acknowledging this Award

- Magen, Y., Gabriel, A.-A., May, D. A., & Karki, P. (2025, 09). The role of crustal mechanics and frictional heterogeneity in postseismic deformation of the 2019 Ridgecrest earthquake. Poster Presentation at 2025 SCEC Annual Meeting.
- Yun, J., Wong, J., Fialko, Y., Gabriel, A.-A., May, D. A., Wallace, L. M., & Williams, C. A. (2025, 09). The 2016 Mw 7.8 Kaikōura, New Zealand, earthquake triggers slow-slip events and delays megathrust earthquakes in rate-and-state friction simulations of the Hikurangi subduction zone. Poster Presentation at 2025 SCEC Annual Meeting.

References

Blewitt, G., Hammond, W., & Kreemer, C. (2018). Harnessing the GPS data explosion for interdisciplinary science. Eos. doi:10.1029/2018eo104623.

Erickson, B. A., & Dunham, E. M. (2014). An efficient numerical method for earthquake cycles in heterogeneous media. J. Geophys. Res. Solid Earth, 119(4), 3290–3316. doi:10.1002/2013JB010614.

Gharti, H. N., Langer, L., & Tromp, J. (2019). Spectral-infinite-element simulations of coseismic and post-earthquake deformation. Geophys. J. Int., 216(2), 1364–1393. doi:10.1093/gji/ggy495.

Jiang, J., et al. (2022). Community-driven code comparisons for three-dimensional dynamic modeling of sequences of earthquakes and aseismic slip. J. Geophys. Res. Solid Earth, 127, e2021JB023519.

Lambert, V., Jiang, J., & Erickson, B. A. (2023). SEAS Benchmark Problems BP7-QD/FD-A/S. SCEC SEAS Working Group.

Lapusta, N., & Liu, Y. (2009). Three-dimensional boundary integral modeling of spontaneous earthquake sequences and aseismic slip. J. Geophys. Res. Solid Earth, 114(B9). doi:10.1029/2008JB005934.

Lapusta, N., Rice, J. R., Ben-Zion, Y., & Zheng, G. (2000). Elastodynamic analysis for slow tectonic loading with spontaneous rupture episodes on faults with rate- and state-dependent friction. J. Geophys. Res. Solid Earth, 105(B10), 23765–23789. doi:10.1029/2000JB900250.

Magen, Y., Baer, G., Ziv, A., Inbal, A., & Nof, R. N. (2024). The postseismic deformation of the 6 July 2019 Mw 7.1 Ridgecrest earthquake from Burst Overlap Interferometry, InSAR, and GNSS. Seismological Research Letters. doi:10.1785/0220240066.

Savage, J. C., & Prescott, W. H. (1978). Asthenosphere readjustment and the earthquake cycle. J. Geophys. Res. Solid Earth, 83(B7), 3369–3376. doi:10.1029/JB083iB07p03369.

Taufiqurrahman, T., Gabriel, A.-A., Li, D., Ulrich, T., Li, B., Carena, S., et al. (2023). Dynamics, interactions and delays of the 2019 Ridgecrest rupture sequence. Nature, 618(7964), 308–315. doi:10.1038/s41586-023-05985-x.

Uphoff, C., May, D. A., & Gabriel, A.-A. (2023). A discontinuous Galerkin method for sequences of earthquakes and aseismic slip on multiple faults using unstructured curvilinear grids. Geophys. J. Int., 233(1), 586–626. doi:10.1093/gji/ggac467.